Long-term triggered seismicity on the Mosha fault by Damavand Volcano, N-Iran, Implications on the seismic hazard of Tehran metropolis

Seyyedmaalek Momeni[1,2*], Raul Madariaga[3]

1. EPFL Geo-Energy Lab – Gaznat Chair on Geo-Energy, EPFL-ENAC-IIC-GEL, Station 18, CH-1015, Lausanne, Switzerland.

2. International Centre for Theoretical Physics (ICTP), Trieste, Italy.

3. Labratoire de Geologie, Ecole Normale Superieure, 75231 Paris Cedex 05, France.

***** Corresponding author, E-mail: maalek.momeni@gmail.com

Abstract

Seismic history of the Mosha fault, the largest and most active fault of Eastern Tehran metropolis (>15 million population) with three documented 6.5<M<7.7 historical earthquakes, and its relation to the Damavand active Volcano, the highest mountain of the Middle East, is investigated. We infer that the seismic activity of the Central Mosha, close to the Damavand, is quite high compared to its western and eastern segments. On May 7, 2020, an Mw5.1 earthquake struck the Central Mosha, some 40 km East of Tehran, 10 km SSW of Damavand crest, and was strongly felt in Tehran. Its rupture is imaged as a patch that nucleates at the depth of 14 km and mostly grows toward the up-dip and to the WNW with an average speed of 2.75 km/s that lasts for ~2.8 s. The rupture is located in a region that presented a relative seismic quiescence compared to its Eastern and Western parts, during the last 14 years, suggesting its partial locking and a heterogeneous distribution of fault frictional strength on this segment of Mosha. Early aftershocks were mainly distributed toward the West and up-dip of the slip model, confirming a strong directivity effect that is also observed from the PGA distribution of the mainshock recorded in the ISMN network. A relatively small stress drop of 2.6 bar is estimated from the extended rupture model, consistent with the relatively large rupture dimension of 9 km for an Mw5.1 earthquake, and suggests the easy rupture expansion on the central segment of the Mosha fault near the Damavand Volcano.

The occurrence of 1930, 1955, and 1983 earthquakes on the Central Mosha, its high microseismic activity, and the 2020 seismic sequence, strongly suggest an effect of Damavand Volcano on the seismicity of the Central Mosha. This is supported by the observed extension of a sill-like Damavand young Magma chamber until this segment of Mosha fault in tomography studies, and, by the observation of thermal areas on the Mosha fault. We suggest that the existing heat raises the pore-pressure on the fault, which decreases the effective normal stress (and ease the rupture nucleation-expansion) unclamping the fault. Damavand may work as a fuse and nucleate earthquakes in which if the rupture grows toward West, will have a strong directivity effect of low-frequency seismic waves that arrive without attenuation in Tehran and affect tall buildings. Besides,

high site amplifications for frequencies up to 16 Hz due to the deep sedimentary basin, mainly in the mid-city of Tehran, will be remarkable for short buildings.

Keywords: Induced seismicity; Earthquake source observations; Earthquake hazards; Volcano seismology; Waveform inversion; Permeability and porosity

1. Introduction

On May 7th, 2020, an M5.1 earthquake occurred in South-Central Alborz mountains just 4 km North of the Mosha fault (hereafter MSH), 10 km South of Damavand Volcano (hereafter DMV), which is situated 45 km East of Tehran city, capital of Iran with over 15 million population (Fig. 1). In spite of its moderate magnitude, it caused two fatalities and several injuries (IRNA news agency). The peak ground acceleration (PGA) of the mainshock was measured 141 cm/s^2 at the close station of the Iranian National Strong Motion Network (ISMN) situated just 12 km Southwest of the epicenter (RDH1, Fig 1b, 6). In terms of mechanism, it exhibits an almost pure strike-slip faulting (Fig. 1, reported by the Iranian Seismological Center (IRSC); Table S1). This event did not produce any surface rupture.

1. Tectonic Settings

The Alborz mountain range is part of the northern boundary between Iran and Eurasia, located South of the Caspian Sea (Fig. 1). It accommodates about 30% of the total 25 mm/y of shortening between Arabia and Eurasia, the remaining being accommodated both by the shortening of the Zagros mountains and by long strike-slip faults in Central Iran (Vernant et al., 2004). The motion between Central Iran and the South Caspian basin is oblique to the belt and involves roughly ~ 5 mm/y of shortening and ~ 4 mm/y of left-lateral strike-slip motion (Vernant et al., 2004, Khorrami et al, 2019). This oblique motion is due to the clockwise rotation of the South Caspian basin (Djamour et al., 2010).

Alborz mountains have deformed during several tectonic episodes. The first corresponds to the collision of the Iranian microplate with Eurasia that occurred during the Late Triassic (i.e., Asserto, 1966; Berberian and King, 1981; Stocklin, 1974). The second was the collision of Arabia with Iran that had the main contribution to the deformation of Alborz. This collision either began ~12 My ago according to the thermochronology of exhumated rocks (Guest et al., 2006 a, b) or before, ~20 My ago based on the sedimentary studies of Ballato et al. (2008, 2011). The second episode is associated with partitioning. It may be started 10 My ago for Hollingsworth et al. (2008), 5 My for Allen et al. (2003), and even younger for Ritz et al., (2006).

The mainshock occurred near the MSH, the longest fault in South-Central Alborz with a length of ~175 km and a left-lateral strike-slip faulting mechanism (Fig. 1), which mostly accommodates the strike-slip component of the Caspian Sea clockwise rotational relative motion (Djamour et al., 2010). This earthquake is the only well-recorded M>5 seismic event near the MSH by the IRSC network.

MSH consists of three segments: The western MSH segment located North of Tehran strikes WNW and is parallel to the eastern segment of the sinistral-reverse Taleghan fault (Guest et al., 2006a, b). The western MSH could be part of a local partitioning system with the Taleghan fault (Guest et al., 2006 a, b) or deactivated in favor of the Taleghan fault (Nazari et al., 2009).

The central MSH strikes WNW with a length of ~80km and branches to the West to the North Tehran fault (NTF, Solaymani et al., 2011). This segment is also a left-lateral strike-slip fault that accumulated ~35 km of total displacement (Guest et al., 2006 a, b). Abbassi and Farbod (2009), however, believe that the NTF is not presently active and suggests instead that the motion occurs on several smaller faults situated southward. A paleoseismological study by Ritz et al., (2012) on a segment of NTF revealed its shallow dip thrusting toward the North (N115°E) and interpreted between 6 and 7 surface-rupturing events with estimated magnitudes between 6.5 to 7.2 that occurred during the past 30 kyrs.

The eastern segment of MSH has a WNW strike and connects to the left-lateral/normal ENE–WSW Firuzkuh fault to the East. It is situated along the Mosha valley and is almost parallel to the Sorkhe fault on its South. This segment has a left-lateral strike-slip motion and dips to the North (Allen et al., 2004; Bachmanov et al., 2004) but with a slight normal component (Ritz et al., 2006). The total sinistral offset is ~35 km (Allen et al., 2003) and the slip rate ~2 mm/y (Ritz et al., 2006). The recent GPS measurements also estimated 1-2 mm/y of left-lateral strike-slip motion on the MSH (Djamour et al., 2010).

It is estimated that the Firuzkuh fault with a late Quaternary estimated slip-rate of 1.1–2.2 mm/yr have had a maximum magnitude of 7.1, involving 1.2 m average displacement, that is expected to occur every 1100– 540 years (Nazari et al., 2014). As the last earthquake on the Firouzkuh fault may be up to 700 years in age, it can be considered as one of the major hazards for future earthquakes.

Tehran is built on a thick sedimentary basin consist of Quaternary alluvial deposits which are the main cause of wave amplification in that area (i.e., Majidnejad et al., 2017; Kamranzad et al., 2020). These sediments have four units: 1-Hezardarreh formation as oldest deposit in Tehran with a thickness of 1200 m that forms an anticline through the northeast-east of Tehran; 2-Kahrizak formation unconformably overlies on the eroded surfaces of Hezardarreh formation with 10-60 m in thickness and maximum dip of 15°; 3-Tehran formation, formed mainly of conglomeratic young alluvial fan deposits. Its thickness can reach 60 m and its bedding is almost horizontal; 4- The last one is the recent alluvium is the youngest stratigraphic unit within the region and its age reaches to Holocene epoch. Its thickness is 10 m. This unit composes of poorly consolidated to unconsolidated cementation with alluvial and fluvial origin (Kamranzad et al., 2020).

Inside Tehran, several active faults have been recognized like Qeytarieh, Lavizan, Pardisan, Chitgar, Garmdare (Talebian et al., 2016, Ritz et al., 2012;

Fig. 4c), among which some have relatively fast slip rates that are estimated > 1mm/yr (e.g., Pardisan). This can have a strong impact on the earthquake hazard assessment of Tehran city and the surrounding region.

DMV is the highest and largest volcano of the Middle-East with an altitude of 5670 m, situated just 50 km Northeast of Tehran city. It is a young, dormant strato-volcano, which is a large intraplate Quaternary composite cone of trachyandesite lava and pyroclastic deposits overlying the active fold and thrust belt of the Central Alborz Mountains. Isotope dating, geological and tomography studies have revealed that the present cone (young Damavand) has been constructed over the last 600 Ky with a dimension of ~80 km^3, a little to the South-Southwest and on an older, eroded edifice of the old Damavand (Davidson et al., 2004, Mostafanejad et al, 2011, Shomali and Shirzad, 2014). Damavand had an average uplift rate of 3 mm/y between the years 2003 to 2010 (Vajedian et al., 2015) which was almost uniformly distributed on the area proposing its sill-like magma chamber (Yazdanparast and Vosooghi, 2014). Thermal areas exist near the MSH (Eskandari et al., 2018), confirming the extension and presence of the DMV Magma chamber toward the MSH (Figs. 4a, 8).

1. **Historical earthquakes of Mosha fault**

Three M>6.5 historical earthquakes are related to the MSH (Ambraseys and Melville, 1982; Berberian, 1994; Berberian and Yeats, 1999; Tchalenko et al., 1974): The 07/06/1665 AD (M6.5) on the eastern segment, 27/03/1830 AD (IX 7.1) on its central segment, and 23/02/958 AD (X 7.7) on its western segment which is also referred partly to the Taleghan fault (Fig. 1a).

Several moderate magnitude earthquakes have also been reported after 1800 AD on the central segment of MSH near DMV: The 1802, 20/06/1811, 1815, and the 02/10/1930 AD Ms 5.2 and 24/11/1955 AD Mb 4.0 earthquakes that occurred just South of the DMV, very close to the 2020 mainshock (Fig. 4a) (Berberian et al., 1993; Nazari et al., 2009).

1. **Instrumental earthquakes of Mosha fault and region**

The instrumental seismicity is widely spread in the region. The EHB catalog (Engdahl et al., 2006) locates most of the seismicity near the Mosha, Firuzkuh, Sorkhe, and Garmsar faults (Fig. 1a). While recent seismic activity recorded by the IRSC network shows a broad distribution of seismicity in the region. Figure 1b shows selected earthquakes of the region that were recorded by the IRSC network since 2006. They are located by at least five stations, have a location error of <3 km, RMS of <0.5 s, and azimuthal gap of <180°. The eastern and central segments of the MSH show more microseismic activity compared to its western segment. A seismic cluster to the East of Tehran city is mostly related to mining activities in that area. The rest of the seismicity is related to the Sorkhe, Eyvanakey, Pishva, Garmsar, Zirab-Garmsar, Firuzkuh, and Robat-Karim faults. Detailed microseismic monitoring on the MSH by a local dense seismic network confirmed its left-lateral strike-slip mechanism with an East-Southeastward oriented fault plane (Tatar et al., 2012; Fig. 4a). Tatar et al.

proposed an average dip of 70° to the North for this fault.

Three moderate magnitude earthquakes with strike-slip mechanisms have been inverted by Momeni, (2012) on the central and eastern segments of the MSH; two of them (#1 and #2) were located South of DMV (Fig. 1b; #1: 20/12/2006 Mw4.2, #2: 26/02/2007 Mw3.6, and #3: 24/04/2008 Mw3.6). However, there was no seismic activity reported for the western MSH segment neither from 1900 to 1996 (Berberian et al., 1993), nor in the recent IRSC catalog (Fig. 1b).

In this study, we first invert the local broadband displacement full waveforms of the 7 May 2020 M5.1 mainshock for its moment tensor. Then, we relocate the mainshock and largest aftershock hypocenters. After, we invert the near field strong-motion displacement wave-fields of the mainshock recorded in the Iranian Strong Motion Network (ISMN), for the Spatio-Temporal evolution of the slip, and investigate its relation to the distribution of early aftershocks, and the seismic history of the MSH. Then, we analyse the frequency content of the mainshock rupture, the f_{max} in the Tehran area, and the stress drop due to the mainshock to better investigate the impact of such earthquakes on the seismotectonics of Tehran city. Finally, we discuss the relation between MSH seismic activity and DMV, and the plausible cause of triggering.

2.Moment Tensor of the 7 May 2020 M5.1 mainshock

The low-frequency full waveforms of the mainshock recorded by eight Iranian broadband seismic network (BIN) stations situated at distances ranging from 84 km to 433 km (Fig. 1a) were inverted to obtain the moment tensor, assuming a point source. The BIN seismic network is maintained by the International Institute of Earthquake Engineering and Seismology (IIEES), Tehran, Iran. More distant stations were excluded from the inversion to keep the maximum possible frequencies of the displacement waves while avoiding the undesirable effects of crustal heterogeneity on the centroid location and moment tensor calculations. The moment tensor inversion was carried out using the latest version of Isola code (Sokos and Zahradnik, 2008). The mean and trend of data were removed and bandpass filtered by fourth-order Butterworth filter between 0.03-0.08 Hz and cut from origin time for a length of 250 s. The Green's functions for the trial point source were computed using the discrete wavenumber (DWN) method (Bouchon, 2003) and the similarity between the observed and calculated waveforms measured by the Variance Reduction (VR) parameter of the Isola code. Details of the inversion procedure are explained in a paper by Momeni and Tatar (2018). We used a velocity model of the area obtained in a detailed microseismic study by Tatar et al., (2012) (Table S2). The trial point sources were grid searched in the activate area (Fig. 2a). The centroid time was searched as well, from 2 s before to 4 s after the origin time with steps of 0.08 s (Fig. 2b). The best wave-form fit was obtained for a point source situated at ~4 km WNW of the hypocenter reported by IRSC, at a depth of 12 km, with a space-time correlation of 85%, proposing that the rupture grew mostly to the West (toward Tehran city). The NW-SE striking nodal plane has a strike/dip of 291°/60° (Figs. 2, 4a), which is steeper than the one obtained by IRSC (52°).

However, that is less steep compared to the GCMT result (68°). The centroid depth could change between 11 km to 16 km, with only a slight change in the waveform-fit (<2%). A total scalar seismic moment of 4.8 E+16 Nm equivalent to Mw 5.1 was computed, which is larger than the GCMT and IRSC results (4.1*E+16 Nm and 2.8*E+16 Nm, respectively.

3.Mainshock/largest Aftershock hypocenters

The mainshock and largest aftershock hypocenters were relocated by visually reading the Pg and Sg crustal phases travel times recorded in the IRSC network and inverting them using the HYPOCENTER code (Lienert and Havskov, 1995). We used a velocity model of the area by Tatar et al., (2012) and applied the station time corrections that were obtained in their study. The obtained hypocenter was situated 4 km North and 2 km East of the Mosha town, at a depth of 14 km (Fig. 4a; Table S1). It is 2 km to the North, 2 km to the East, and 3 km deeper than the IRSC hypocenter.

For the M4.1 aftershock, the obtained hypocenter was located 2 km south and 4 km West of the mainshock hypocenter and at a depth of 9 km (Fig. 4a). The latter is almost 1 km northwest of the IRSC reported hypocenter and is 3 km shallower than their result.

We stress that the hypocenter locations of the earthquakes in the study region provided by the BIN seismic network have higher uncertainty compared to IRSC reported locations. This is due to a relatively sparse coverage of the BIN network (only 3 stations in the distance of 100 km from the earthquake). While the IRSC network had 10 stations in the same distance from the source. The IIEES reported hypocenter for the mainshock is located at 2 km to the West, 3 km to the South, and 4 km shallower than our location. Their located hypocenter for the largest aftershock is situated in 2 km to the West, 3 km to the South, and 1 km deeper than our result.

4. Modeling the rupture process of the mainshock

4.1. Inversion Methodology

To obtain the spatial and temporal evolution of the slip for the mainshock, we invert near-field strong-motion displacement time-series recorded by ten three-components SSA-2 Kinemetrics digital accelerometers from the ISMN network. The stations are located at distances ranging between 4 km and 60 km from the rupture area (Fig. 1b). The acceleration data is integrated twice to displacements. The mean and trend of the waveforms are corrected and the horizontal components are rotated to an NS/EW coordinate system. The waveforms cut using a time window of 25.6 s after the respective origin time (Fig. 3d). The data were band-pass filtered using a Butterworth one-pass causal filter in the frequency band 0.08-0.7 Hz. We observed some low-frequency noise below 0.08 Hz. Also, the upper limit of the frequency band is chosen based on the resolution of the crustal velocity model and simplifications assumed in the used model.

The processed data has inverted for the rupture evolution using the elliptical sub-fault approximation method (i.e., Ruiz and Madariaga, 2013; Twardzik et al., 2012; Ruiz et al., 2019; Momeni et al., 2019). It approximates the rupture distribution with a few elliptical patches on a planar fault, and, has the advantage of reducing the number of parameters of inversion in comparison to the more commonly used rectangular sub-faults parametrization. Each of the elliptical slip patches is described by just nine parameters: five to define its geometry. The other four parameters to describe the rupture process, which are slip amplitude, slip duration, slip direction, and onset time. While this method is not suited to retrieve fine details of the rupture process, it focuses on the more robust features of the source.

Proper geometry is grid-searched for the mainshock near the two nodal planes obtained in section 2 (Fig 3b). One and two elliptical patch(s) were investigated to estimate the rupture process. During the inversions, for each of the tested geometries, we consider a wide range of source parameters (see Figures S2 to S11). The inversions were carried out using the Neighborhood Algorithm (Sambridge, 1999) to search for the rupture model that fits best the strong-motion displacements. The Green's Functions were computed using AXITRA (Cotton and Coutant, 1997), a program that is based on a discrete wavenumber method (Bouchon, 2003), and adopting Tatar et al., (2012) velocity model. For each inversion, the hypocenter is allowed to move ±1 km on the fault plane along strike and dip to allow small corrections for errors on the origin time. Up to 500 iterations were applied during inversions, and each iteration had 35 different trial rupture models to ensure convergence (for more details see Figures S2 to S11).

4.2 Rupture process of the Mainshock (Mw5.1)

The obtained hypocenter in section-3 has been used as the initiation point of rupture, and different trial planar rupture geometries were tested in the inversion using one elliptical slip patch to find the optimum geometry based on waveform fit to the strong-motion records. The WNW striking nodal plane provides a better wave-fit of 58%, suggesting that the rupture occurred on the MSH. The geometries close to the NW striking nodal plan were investigated as well, to find a rupture plane that provides the best waveform-fit to the data (Fig. 3b). The preferred geometry has a strike/dip = 292°/60°. This geometry is close to the general NW strike of the MSH in this area. However, the dip angle is 10 degrees less than the average dip of 70° proposed by Tatar et al., (2012) for the MSH.

4.2.1. Rupture process using one elliptical slip patch

Ten final rupture models resulted from different inversions of the near field displacement waveforms are evaluated (see Fig. 3a; Table S3). They describe the mainshock slip using one elliptical slip patch. These rupture models were calculated on a planar fault with a strike/dip of 292°/60°N and with the hypocenter obtained in section-3. They have a minimum wave misfit of ~42%. Most of the misfit is due to the late part of the displacement fields which mainly contain the

surface waves and site effects (see figures S2 to S11). For all of these models, the slip extends to the West of the hypocenter with large values located at depths ranging between 13 km to 10 km. This range is within our obtained depth range for the maximum waveform correlation in the moment tensor inversion as well as the IRSC result. The rupture has a left-lateral strike-slip mechanism (rakes =14°-18°) and does not reach the surface.

All the models had sub-shear rupture speeds between 2.2 km/s to 2.8 km/s (Vs=3.5 km/s) and almost the same duration, between 2.1 s to 2.8 s. The rise time changes between 0.02s to 0.26s. Models with higher rise times exhibit mostly higher rupture speeds, which is consistent with the results of dynamic simulations from Schmedes et al. (2010). The maximum slip changes from 3 cm to 9 cm, depending on the rupture dimension.

The inversions converge to a seismic moment release between 3.8e+16 Nm to 4.3e+16 Nm, which are smaller than the estimated scalar moment obtained by regional waveform inversion (4.8 e+16 Nm). We stress that the low-frequency noises in the strong motions limited inversion to use frequencies below 0.08 Hz. While in section 2, we use frequency ranges down to 0.03 Hz. All the rupture models can satisfy the strong motion data. We make an average of the ten final models as our preferred model. This rupture model shows nucleation at the depth of ~14 km (Fig. 4a). The slip mostly extends toward the west and to the shallow depths with an average speed of 2.75 km/s. The maximum slip is estimated as ~4 cm between depths ranging from 13km to 11km. The rupture lasts for ~2.8 s and releases a total scalar seismic moment of 4.04 E+16 Nm equal to Mw 5.0. That is less than the point-source moment tensor results in section 2. The maximum slip is situated 2.5 km West and ~0.5 km South of the hypocenter and at a depth of 12 km. The rupture stops at a depth of 10 km. The rupture length of ~9 km for an M5.0 event is remarkable, proposing its comfort extension.

4.2.2. Rupture process using two elliptical slip patches

When two elliptical slip patches are used in the inversion, the misfit of the kinematic rupture models reduces to a minimum value of 39% which is not a strong improvement in the wave-fit. So, the model with one slip patch is enough to estimate the mainshock rupture.

5. Aftershocks and their correlation with the mainshock rupture

27 M>=2.5 aftershocks located in the IRSC network within the first 45 days after the mainshock (Fig. 4a). They have location errors of <3 km, an azimuthal gap of <180°, and an RMS of < 0.5 s. They concentrated in front of the mainshock rupture direction. All of the aftershocks are at depths between 8 km to 14 km. Tatar et al., (2012) also located most of the microseisms on the central segment of MSH and at depths between 10 km to 15 km.

The largest (M4.1) aftershock of the 2020 sequence (occurred on May 27) is located right in front of the mainshock rupture, where it was arrested, suggest-

ing that the aftershock was a continuation of the same slipped area. Its focal mechanism is almost the same as the mainshock (Fig. 4a). There are two other aftershocks far from the mainshock slip: one near the DMV, and the other in the area where the 24/11/1955 earthquake occurred.

6. Seismicity along the Mosha fault from 1996

Reliable earthquake locations by the IRSC seismic network in East of Tehran started in 1996. However, the IRSC network was relatively sparse until 2005 so that there are only 47 well-located earthquakes in the distance of 5 km from the MSH (Fig. 5 a, b). The selected earthquakes have location errors of < 5km, RMS of < 0.5 s, azimuthal gaps of $< 180°$, and are located by at least six stations. The mentioned events are mostly distributed on the Central segment of the MSH with a considerable concentration near the DMV. As the IRSC seismic network has improved from 2006, in both terms of magnitude completeness and location accuracy, 60 M>=2.5 earthquakes were located by them in the distance of 5 km from the MSH until the May 7th mainshock (Fig. 5 a, b, Table S4). This group of earthquakes has a smaller location error of <3 km, azimuthal gap of $< 180°$, and RMS of < 0.5 s. This seismicity is also concentrated on the Central segment of MSH, near the DMV. While, the Eastern segment also shows seismicity on its eastern termination, and the Western one is almost silent.

After the 2020 mainshock, 27 M>=2.5 aftershocks were located by the IRSC network, 28 of them were situated in the same distance range of 5 km from the central segment of Mosha (Fig. 5 b, Table S5). It is evident from Figure 5 c, d that the M5.1 mainshock rupture and its early aftershocks (45 days) occurred in a part of MSH that had a much lower seismic activity compared to its neighboring segments. As the located earthquakes after 2006 have better locations, we decided to compute the cumulative scalar seismic moments of the earthquakes that occurred after 2006, to investigate the seismic energy release behavior along the fault. The cumulative scalar seismic moment plot shows three peaks of seismic energy: two of them on the East and West of the M5.1 rupture on the central segment, and one near the eastern termination of the fault (Fig. 5 b, c). These peaks are mostly related to three events that occurred on 20/12/2006 Mw4.2 (#1), 26/02/2007 Mw3.6 (#2), and 4/04/2008 Mw3.6 (#3), and their moment tensors were inverted by Momeni, (2012) (Fig. 1b).

The early aftershocks were surrounded by the two peaks of cumulative scalar seismic moment release of earthquakes from 2006 until the M5.1 mainshock (Fig. 5c). After the mainshock, the cumulative scalar seismic moment plot shows a big peak in the mainshock slip area and its related aftershocks (Fig. 5d) that has a comparable amplitude to the scalar seismic moment release from the 1930 M5.2 earthquake.

7. Discussion

The seismicity of the MSH is investigated from documented historical earthquakes previous to 22 June 2020. Three M>=6.5 historical earthquakes cover all the MSH segments. However, instrumental seismicity is relatively poor. The

EHB catalog (Engdahl et al., 2006) shows three earthquakes near the Eastern and Central segments of MSH, close to DMV. The GCMT catalog shows two 5<M<5.3 earthquakes on the Central and Eastern segments of the MSH. The IRSC network earthquake catalog has improved from 2006 in terms of completeness. They show 67 M>=2.5 earthquakes within a distance of 5 km from the fault before the 2020 mainshock. Most of this seismicity concentrated on the Central segment of MSH, South of the DMV. Three peaks are observable in the cumulative Scalar Seismic Moment chart of these earthquakes (Fig. 5c). Interestingly, the central peaks that are mostly related to the 2006 and 2007 earthquakes, coincide with the estimated rupture areas during the Ms 5.2 1930 and Mb 4.0 1955 earthquakes. A possible explanation is that they are late aftershocks of these earthquakes. The Western one is close to thermal areas reported by Eskandari et al. (2018). A low-velocity region has obtained Southwest of DMV that extended until the MSH down to the depth of 15 km in a tomography study by Mostafanejad et al. (2011) (Fig. S1a). The observed thermal activities in the same area are probably due to the existence of some branches of the DMV magma chambers in that area which was also suggested by Eskandari et al. (2018).

The rupture process and the fault geometry of the 7 May 2020 M5.1 Damavand earthquake was investigated by inverting both the local broadband seismic data for the moment tensor and the near-field strong-motion displacement time series for its extended rupture model. The mainshock occurred on the central segment of the MSH: It nucleated ~15 km SSW of the DMV crest and at a depth of ~14 km. The rupture is estimated in an elliptical patch with a major-minor axis of 5 km-3.6 km. It evolves mostly toward the Northwest along strike and to the up-dip direction at a sub-shear speed of ~2.75 km/s for 2.8 s. The estimated geometry is ~WNW (292°) strike and ~60° dip to the North. The obtained scalar seismic moment by point-source moment tensor inversion is 4.8 e+16 Nm while using an extended rupture model, this value reduces to 4.04 e+16 Nm, suggesting the release of some of the scalar seismic moment at relatively lower frequencies between 0.03 Hz to 0.08 Hz.

The interpolated PGA from 33 recorded stations of the ISMN network suggest a west-northwestward directivity, which is to some extent consistent with our source model showing a westward directivity (Fig. 4a). For each station, peak values of the geometric average of the two horizontal components of strong motions are considered as horizontal PGA. The damping observed in PGA in the center of Tehran is interpreted as attenuation due to the deepest part of the sedimentary basin (see Majidnejad et al., 2017). The Fourier spectra of the strong motion data for stations FRK3 and LVS1 that have negligible site effect, show the low-frequency content of this event with a corner frequency of 1 Hz. Far-field Brune models for an M5.1 earthquake is estimated in Tehran region (Brune, 1970) in which source slip patch radius is roughly 4.3 km, S-wave velocity is 3.5 km /s, and ρ is equal to 1.5 (Figs. 6 and 7). The f_{max} is obtained from the smoothed spectra (see Konno & Ohmachi, 1998; Figures 6, 7, S12, S13) in the ranges between 6 Hz to 16 Hz in the Tehran region. Such difference

is mainly related to the site attenuation (i.e., scattering and dissipation) (see Gomberg et al., 2012; Hanks, 1982).

The stress drop has obtained 2.6 bar from the extended rupture model, posing roughly a circular slip patch with a radius of 4.3 km, and a scalar seismic moment of 4.8 e+16 Nm (see Madariaga, 1977). An empirical relation between scalar moment and stress drop by Ide and Beroza, (2001) suggests a stress drop of ~10 bars for an M5.1 earthquake. The obtained relatively low stress drop is consistent with the relatively large rupture length. We note that the obtained rupture length (estimated between 7 km to 9 km) is relatively large for such a magnitude earthquake (for example see Momeni et al., 2019 for a rupture length of ~12 km estimated for an Mw6.5 earthquake; and Vicic et al., 2020 with rupture length of ~4 km for an Mw5.1 earthquake).

The mainshock exhibits a left-lateral strike-slip mechanism (Rake=14°) the same as the general mechanism of MSH proposed by Tatar et al., (2012), a geodetic study of Djamour et al., (2010), and geological-paleoseismological studies by Nazari et al., (2009) and Solaymani-Azad et al., (2011). A maximum slip of ~3 cm was estimated between depths of 12 km and 11 km. The rupture stopped at a depth of 8 km.

The mainshock rupture and the early aftershocks occurred between the two peaks of cumulative scalar seismic moments on the MSH, proposing that this part of the fault was somehow locked compared to two other neighbors that experienced the 1930 and 1955 earthquakes.

The aftershocks were distributed toward the West and up-dip, consistent with the main rupture direction and general orientation of the MSH. The largest aftershock with M4.1 occurred 20 days after the mainshock with a left-lateral strike-slip mechanism, the same as the mainshock. Aftershocks surrounding the mainshock slipped area (Figs. 4a, 5), is a consistent feature of large earthquakes (see Henry and Das, 2002).

The 2020 seismic activity occurred at a depth range between 15 km to 8 km, where Tatar et al. (2012) also detected most of the microearthquakes. This range is almost the same as the upper-crystalline layer of the velocity model obtained by Abbasi et al. (2010) for the region. This relatively thick and deep part of the seismogenic layer may have the potential for the production of large earthquakes with low-frequency contents that can reach Tehran with less damped seismic energy and affect the tall buildings, the same as the 7^{th} May 2020 M5.1 mainshock.

The smooth geometry of the central segment of MSH may facilitate the rupture expansion on it. Occurrence of the 1930 (Ms 5.2), 1955 (Mb 4.0), 1983 (Mw 5.3), and 2020 (Mw 5.1) earthquakes in the South of the DMV, together with its seismic activity from 2006, suggest a strong relationship between the volcanic activity of DMV and relatively high seismicity rate of the central segment of the MSH. Also, most of the microseismic activity and larger microearthquakes were reported by Tatar et al. (2012) on the central segment of MSH, just to the

South of DMV between longitudes from 51.75 E to 52.2 E, while their seismic network was well-distributed on the two other segments of MSH.

Previous studies suggested the existence of a hot young sill-like magma chamber of DMV in the Southwest of its current crater (i.e. Mostafanejad et al., 2011; Shomali and Shirzad, 2014; Yazdanparast and Vosooghi, 2014; Eskandari et al., 2018). While the old magma chamber of Damavand is detected toward the North-Northeast of the crater and is detected as a cooled high-velocity dike-like structure (Mostafanejad et al., 2011). The existing young magma chamber may increase the pore pressure on the left-lateral strike-slip MSH which consequently decreases the effective normal stress on it and facilitates the rupture nucleation-expansion (Fig. 8). Such phenomena have been widely observed and reported mostly for Strike-slip and Normal faulting mechanisms (i.e. Saar and Magna, 2003, Goebel et al., 2017, Scuderi et al., 2017, Johann et al., 2018, Eaton and Schultz, 2018, Benson et al., 2020). On the other hand, such a mechanism may not allow considerable accumulation of strain on this part of the MSH near DMV (i.e. Yagi et al., 2016).

The 2020 M5.1 earthquake is the largest well-recorded event on the MSH after the 1983 event. This segment of the MSH has experienced the 1830 IX 7.1 historical earthquake. All of the evidences indicate that the 2020 M5.1 mainshock and recent seismicity of the central segment of MSH are related to the existence/activity of the magma chamber of DMV. We also stress that 1930, 1955, and 1983 earthquakes on the South of DMV might have happened as a result of the same unclamping mechanism due to the existing high pore pressure.

Compared to the Central segment of Mosha, the Western segment that is closer to Tehran city is silent. However, GPS studies confirm its lower deformation rate (1mm/y, Djamour et al., 2010). The occurrence of earthquakes like the 2012 Ahar-Varzaghan doublet (Mw 6.5 and Mw 6.3) with almost no detected seismic activity in the IRSC network before the mainshock and low deformation rate (i.e., Momeni et al., 2019) highlights the importance of a detailed seismic-geodetic study on the Western segment of MSH that will affect the seismic hazard of that region, and especially Tehran city. Also, the Eastern segment of MSH shows seismic activity which highlights its importance as another potential segment of the MSH for future large earthquakes.

8. Conclusion

We infer that the seismicity of the central segment of the MSH in the South of DMV is excited by the existing young sill-like magma chamber of DMV between them. The eastern segment shows lower seismic activity and the western one is almost quiet. We suggest that the transferred heat by the magma chamber to the fractured area of the MSH raises the pore pressure that consequently decreases the effective normal stress on this part of the MSH and triggers the rupture nucleation-expansion. The two peaks of scalar seismic moment release are observed on both sides of the 7 May 2020 M 5.1 mainshock, suggesting its partial locking. However, the occurrence of several small to moderate magnitude

earthquakes on this segment of MSH suggests a heterogeneous distribution of stress on it. This means, both the heterogeneous distribution of fault plane strength and raised pore-pressure due to temperature may play roles in the central segment of the MSH near DMV.

The PGA distribution of strong motions in near-field and Tehran and the obtained rupture model for the mainshock reveal its directivity toward the West (Tehran). The corner frequency is estimated at 1 Hz which is consistent with the Brune (1970) model. F_{max} is estimated between 6 Hz to 16 Hz in the Tehran region. The obtained F_{max} is close to the averaged value reported in a study by Haghshenas and Bard, (2007) (10 Hz). These high-frequency waves may be due to the amplification caused by the sedimentary basin beneath Tehran. The Amax frequencies change from 2 Hz to 17 Hz. However, most of stations inside Tehran show relatively similar frequencies for Amax between 2 Hz and 6 Hz (Fig. 4c, Table S7). Negligible attenuation of low-frequency signals (< 1 Hz) (related to the source rupture) in Tehran region is observed (see Figs. 6, 7).

In terms of rupture dynamics, DMV can work as a fuse and nucleate earthquakes on the MSH, for which if the rupture grows toward the West, it will cause a strong directivity effect for that earthquake toward Tehran megacity, similarly to the 7 May 2020 M 5.1 earthquake (Fig. 4b, c). The western segment of MSH that is the closest segment to the Tehran metropolis may be fully locked, as it has almost no seismic activity, but GPS measurements show a deformation rate of 1 mm/y for it, and a locking depth of 16 km is suggested. This segment did not rupture since the 958 AD M~7.7 Taleghan-Mosha historical earthquake.

9. Data and Resources

The earthquakes data are available through the Iranian Seismological Center (IRSC) network website (http://irsc.ut.ac.ir). The strong motion waveforms are available from the Iranian Strong Motion Network (ISMN) website (http://smd.bhrc.ac.ir). The supplementary data includes velocity model of the area, earthquakes hypocenters information, moment tensor inversion result of section 2, and rupture inversion tests-results of section 4.

10. Acknowledgements

This research did not receive any specific grant from funding agencies in the public, commercial, or not-for-profit sectors. We thank the editor Victor M. Cruz-Atienza, Hamid Nazari, and an anonymous reviewer for their constructive comments that improved the manuscript. We thank IIEES, IRSC, and ISMN networks for providing the seismic and strong motion data. Figures plotted using Generic Mapping Tools (GMT) (http://gmt.soest.hawaii.edu/), personal codes in Matlab environment (https://www.mathworks.com), and Paraview software (https://www.paraview.org).

11. References

Abbassi, M.R. & Farbod, Y., 2009. Faulting and folding in quaternary deposit of Tehran's piedmont (Iran). Journal of Asian Earth Sciences, **34**, 522–531.

https://doi.org/10.1016/j.jseaes.2008.08.001

Allen, M.B., Ghassemi, M.R., Sharabi, M. & Qoraishi, M., 2003. Accommodation of late Cenozoic oblique shortening in the Alborz Range, northern Iran. Journal of Structural Geology, **25**, 659–672. https://doi.org/10.1016/S0191-8141(02)00064-0

Allen, M., Jackson, J. & Walker, R., 2004. Late Cenozoic reorganisation of the Arabia– Eurasia collision and the comparison of short-term and long-term deformation rates. Tectonics, **23**, TC2008. doi:10.1029/2003TC001530.

Ambraseys, N.N. & Melville, C.P., 1982. A History of Persian Earthquakes, Cambridge Univ. Press.

Asserto, R., 1966. Geological map of upper Djadjurd and Lars valley, (central Alborz, Iran). Inst. Geol. Univ. Milano, Serie G., 232. Spec. Pub.

Ballato, P., Nowaczyk, N.R., Landgraf, A., Strecker, M.R., Friedrich, A. & Tabatabaei, S.H., 2008. Tectonic control on the sedimentary facies pattern and sediment accumulation rates in the Miocene foreland basin of the Southern Alborz Mountains, Northern Iran. Tectonics **27**, TC6001. doi:10.1029/2008TC002278.

Ballato, P., Uba, C.E., Landgraf, A., Strecker, M.R., Sudo, M., Stockli, D.F., Friedrich, A. & Tabatabaei, S.H., 2011. Arabia–Eurasia continental collision: Insights from late Tertiary foreland-basin evolution in the Alborz Mountains, Northern Iran. Geological Society of America Bulletin **123**, 106–131. https://doi.org/10.1130/B30091.1

Bachmanov, D.M., Trifonov, V.G., Hessami, K.T., Kozhurin, A.I., Ivanova, T.P., Rogozhin, E.A., Hademi, M.C. & Jamali, F.H., 2004. Active faults in the Zagros and central Iran. Tectonophysics **380**, 221–241. https://doi.org/10.1016/j.tecto.2003.09.021

Benson, P.M., Austria, D.C., Gehne, S., Butcher, E., Harnett, C.E., Fazio, M., Rowley, P. & Tomas, R., 2020. Laboratory simulations of fluid-induced seismicity, hydraulic fracture, and fluid flow, Geomechanics for Energy and the Environment 24, 100169. https://doi.org/10.1016/j.gete.2019.100169.

Berberian, M. & King, G.C.P., 1981. Towards a paleogeography and tectonic evolution of Iran. Canadian Journal of Earth Sciences **18**, 210–265. https://doi.org/10.1139/e81-019

Berberian, M., Ghorashi, M., Arjangravesh, B. & Mohajer-Ashjaie, A., 1993. Seismotectonic and earthquake-fault hazard investigations in the great Ghazvin Region, Geological Survey of Iran, Report no. 57, 84pp (in Farsi), GSI, Tehran, Iran.

Berberian, M., 1994. Natural hazards and the first earthquake catalog of Iran, vol. 1: Historical hazards in Iran prior 1900, I.I.E.E.S. report.

Berberian, M., 1997. Seismic sources of the Transcaucasian historical earthquakes, in Historical and Prehistorical Earthquakes in the Caucasus, pp. 233–311, eds., Giardini, S. and Balassanian, S., Kluwer Academic Publishing, Dordrecht, Netherlands. https://doi.org/10.1007/978-94-011-5464-2_13

Berberian, M. & Yeats, R.S., 1999. Patterns of historical earthquake rupture in the Iranian Plateau. Bulletin of the Seismological Society of America **89**, 120–139.

Bouchon, M., 2003. A Review of the Discrete Wavenumber Method, 2003, Pure appl. geophys. **160**, 445–465.

Brune, J. N., 1970. Tectonic stress and the spectra of seismic shear waves from earthquakes, *J. Geophys. Res.*, **75**(26), 4997– 5009, doi:10.1029/JB075i026p04997.

Cotton, F. & Coutant, O., 1997. Dynamic stress variations due to shear faults in a plane-layered medium, Geophys. J. Int., **128**, 676–688. https://doi.org/10.1111/j.1365-246X.1997.tb05328.x

Davidson, J., Hassanzadeh, J., Berzins, R., Stockli, D. F., Bashukooh, B., Turrin, B. & Pandamouz, A., 2004. The geology of Damavand volcano, Alborz Mountains, northern Iran. *GSA Bulletin*; **116** (1-2), 16–29. doi: https://doi.org/10.1130/B25344.1.

Djamour, Y., Vernant, P., Bayer, R., Nankali, H.R., Ritz, J.F., Hinderer, J., Hatam, Y., Luck, B., Le Moigne, N., Sedighi, M. & Khorami, F., 2010. GPS and gravity constraints on continental deformation in the Alborz mountain range, Iran, Geophys. J. Int, **181**, 1287-1301. https://doi.org/10.1111/j.1365-246X.2010.04811.x

Eaton, D.W., & Schultz, R., 2018. Increased likelihood of induced seismicity in highly overpressured shale formations, Geophysical Journal International, 214(1), 751–757, https://doi.org/10.1093/gji/ggy167.

Engdahl, E.R., Jackson, J.A., Myers, S.C., Bergman, E.A. & Priestley, K., 2006. Relocation and assessment of seismicity in the Iran region. Geophys. J. Int. 167, 761–778. https://doi.org/10.1111/j.1365-246X.2006.03127.x

Eskandari, A., Amini, S., De Rosa, R. & Donato, P., 2018. Nature of the magma storage system beneath the Damavand volcano (N. Iran): An integrated study. S0024 4937(17)30423-1. doi: 10.1016/j.lithos.2017.12.002.

Goebel, T.H.W., Weingarten, M., Chen, X., Haffener, J. & Brodesky, E.E., 2017. The 2016 Mw5.1 Fairview, Oklahoma earthquakes: Evidence for long-range poroelastic triggering at >40 km from fluid disposal wells, Earth and Planetary Science Letters, **472**, 50-61. DOI: 10.1016/j.epsl.2017.05.011

Gomberg, J., Creager, K., Sweet, J., Vidale, J., Ghosh, A., & Hotovec, A., 2012. Earthquake spectra and near-source attenuation in the Cascadia subduction zone, *J. Geophys. Res.*, 117, B05312, doi:10.1029/2011JB009055.

Guest, B., Axen, G.J., Lam, P.S. and Hassanzadeh, J., 2006a. Late Cenozoic shortening in the west-central Alborz Moutains, northern Iran, by combined conjugate strike–slip and thin-skinned deformation. Geosphere **2**, 35–52. https://doi.org/10.1130/GES00019.1

Guest, B., Stockli, D.F., Grove, M., Axen, G.J., Lam, P.S. & Hassanzadeh, J., 2006b. Thermal histories from the central Alborz Mountains, northern Iran: implications for the spatial and temporal distribution of deformation in northern Iran. GSA Bulletin **118**, 1507–1521. https://doi.org/10.1130/B25819.1

Haghshenas, E. & Bard, P.Y., 2007. Strong Motion Simulation in Tehran Using Empirical Green Function Method, Journal of Seismology and Earthquake Eengineering: 2007, **9**, 3, 137-152.

Hamzeloo, H., Vaccari, F. & Panza, G. F., 2007. Towards a reliable seismic microzonation in Tehran, Iran, Engineering Geology, **93,** 1–16.

Hanks, T.C., $f_{\max}$. *Bulletin of the Seismological Society of America* 1982;; 72 (6A): 1867–1879.

Henry, C., & Das, S., 2002. The Mw 8.2, 17 February 1996 Biak, Indonesia, earthquake: Rupture history, aftershocks, and fault plane properties, Journal of Geophysical Research: Solid Earth, **107**, 148-227, https://doi.org/10.1029/2001JB000796

Hollingsworth, J., Jackson, J., Walker, R. and Nazari, H., 2008. Extrusion tectonics and subduction in the eastern South Caspian region since 10 Ma. Geology **36**, 763–766. https://doi.org/10.1130/G30529Y.1

Ide, S. & Beroza, G. C., 2001. Does apparent stress vary with earthquake size?, Geophysical research letters, 28, 17, 3349-3352.

Johann, L., Shapiro, S.A. & Dinske, C., 2018. The surge of earthquakes in Central Oklahoma has features of reservoir-induced seismicity. Sci Rep 8, 11505. https://doi.org/10.1038/s41598-018-29883-9.

Kamranzad, F., Memarian, H. & Zare, M., 2020, Earthquake risk assessment for Tehran, Iran. International Journal of Geo-Information, 9, 430; doi:10.3390/ijgi9070430

Khorrami, F., Vernant, P., Masson, F., Nilfouroushan, F., Mousavi, Z., Nankali, H., Saadat, S.A., Walpersdorf, A., Hosseini, S., Tavakoli, P., Aghamohammadi, A. & Alijanzade, M., 2019. An up-to-date crustal deformation map of Iran using integrated campaign-mode and permanent GPS velocities, *Geophysical Journal International*, 217, 2, 832–843, https://doi.org/10.1093/gji/ggz045

Konno, K, & T. Ohmachi, T., 1998. Ground-motion characteristics estimated from spectral ratio between horizontal and vertical components of microtremor, Bull. Seismol. Soc. Am. 88, 228–241.

Lienert, B.R. & Havskov, J., 1995. A computer program for locating earthquakes both locally and globally, Seismol. Res. Lett., **66**, 26–36.

https://doi.org/10.1785/gssrl.66.5.26

Majidnejad, A., Zafarani, H. & Vahdani, S., 2017. Dynamic simulation of ground motions from scenario earthquakes on the North Tehran Fault, Geophysical Journal International, **209,** 434–452, doi: 10.1093/gji/ggx017

Mostafanejad A, Shomali ZH & Mottaghi AA., 2011. 3-D velocity structure of Damavand volcano, Iran, from local earthquake tomography. J Asian Earth Sci **42**, 1091–1096. doi: 10.1016/j. jseaes.2011.03.011.

Momeni, S.M., 2012. Seismicity and Seismotectonic of the Garmsar region. Master thesis in Persian. International Institute of Earthquake Engineering and Seismology, pp. 132.

Momeni, S.M. & Tatar, M., 2018. Mainshocks/aftershocks study of the August 2012 earthquake doublet on Ahar-Varzaghan complex fault system (NW Iran). Physics of the Earth and Planetary Interiors, **283**, 67-81. https://doi.org/10.1016/j.pepi.2018.08.001

Momeni, S.M., Aoudia, A., Tatar, M., Twardzik, C. & Madariaga, R., 2019. Kinematics of the 2012 Ahar–Varzaghan complex earthquake doublet ($M_{\rm w}$6.5 and $M_{\rm w}$6.3), Geophysical Journal International, **217**, 2097–2124. https://doi.org/10.1093/gji/ggz100.

Nazari, H., Ritz, J.-F., Shafei, A., Ghassemi, A., Salamati, R., Michelot, J.-L. & Massault, M., 2009. Morphological and paleoseismological analyses of the Taleghan fault, Alborz, Iran. Geophysical Journal International. **178**, 1028-1041, doi:10.1111/j1365-246x.2009.04173. x.

Nazari, H., Ritz, J.-F., Salamati, R., Shahidi, A., Habibi, H., Ghorashi, M. & Bavandpur, A.K. 2010, Distinguishing between fault scarps and shorelines: the question of the nature of the Kahrizak, North Rey and South Rey features in the Tehran plain (Iran). Terra Nova, 22: 227-237. https://doi.org/10.1111/j.1365-3121.2010.00938.x

Nazari H, Ritz J-F, Walker R, Salamati R, Rizza M, Patnaik R, Hollingsworth J, Alimohammadian H, Jalali A. & Firouz AK., 2014. Palaeoseismic evidence for a medieval earthquake, and preliminary estimate of late Pleistocene slip-rate, on the Firouzkuh strike-slip fault in the Central Alborz region of Iran. J Asian Earth Sci, 82:124–35.

Ritz, J.-F., Nazari, H., A. Ghassemi, A., Salamati, R., Shafei, A., Solaymani, S. & Vernant, P., 2006. Active Transtension inside Central Alborz: a new insight of the Northern Iran–Southern Caspian Geodynamics. Geology **34**, 477–480. https://doi.org/10.1130/G22319.1

Ritz, J.F., Nazari, H., Balescu, S., Lamothe, M., Salamati, R., Ghassemi, A., Shafei, A., Ghorashi, M. & Saidi, A., 2012. Paleoearthquakes of the past 30,000 years along North Tehran Fault (Iran), JOURNAL OF GEOPHYSICAL RESEARCH, 117, B06305, doi:10.1029/2012JB009147, 2012

Schmedes, J., Archuleta, R.J. & Lavallee, D., 2010. Correlation of earthquake source parameters inferred from dynamic rupture simulations, J. geophys. Res., **115**, B03304, doi: 10.1029/2009JB006689.

Solaymani, S., Ritz, J.-F. & Abbassi, M., 2011. Analyzing the junction between the Mosha and the North Tehran active faults. Tectonophysics **497**, 1–14.

Shomali, Z. H. & Shirzad, T., 2014. Crustal structure of Damavand volcano, Iran, from ambient noise and earthquake tomography. Journal of Seismology **19**, 191-200. https://doi.org/10.1007/s10950-014-9458-8

Stocklin, J., 1974. Possible ancient continental margin in Iran. In: Burke, C., Drake, C. (Eds.), Geology of Continental Margins. Springer-Verlag, New York, 873–877. https://doi.org/10.1007/978-3-662-01141-6_64

Ruiz, S., & Madariaga, R., 2013. Kinematic and dynamic inversion of the 2008 northern Iwate earthquake, Bull. Seismol. Soc. Am., **103**(2A), 694–708, doi: 10.1785/0120120056.

Ruiz, S., Ammirati, J.B., Leyton, F., Cabrera, L., Potin, B. & Madariaga, R.,2019. The January 2019 (Mw 6.7) Coquimbo Earthquake: Insights from a Seismic Sequence within the Nazca Plate. *Seismological Research Letters*; **90** (5): 1836–1843. https://doi.org/10.1785/0220190079

Saar, M.O. & Manga, M., 2003. Seismicity induced by seasonal groundwater recharge at Mt. Hood, Oregon, Earth and Planetary Science Letters, **214**, 605-618. https://doi.org/10.1016/S0012-821X(03)00418-7

Sambridge, M., 1999. Geophysical inversion with a neighborhood algorithm—I. Searching a parameter space, Geophysical. J. Int., **138**, 479–494. https://doi.org/10.1046/j.1365-246X.1999.00876.x

Scuderi, M.M., Collettini, C. & Marone, C., 2017. Frictional stability and earthquake triggering during fluid pressure stimulation of an experimental fault, Earth and Planetary Science Letters, **477**, 84-96. https://doi.org/10.1016/j.epsl.2017.08.009

Sokos, E. & Zahradník, J., 2008. ISOLA a Fortran code and a Matlab GUI to perform multiple-point source inversion of seismic data, Computers and Geosciences, **34**, 967-977. https://doi.org/10.1016/j.cageo.2007.07.005

Talebian, M., Copley, A., Fattahi, M., Ghorashi, M., Jackson, J., Nazari, H., Sloan, R., & et al. 2016. Active faulting within a megacity: the geometry and slip rate of the Pardisan thrust in central Tehran, Iran. *Geophysical Journal International, 207* (3), 1688-1699. https://doi.org/10.1093/gji/ggw347

Tatar, M., Hatzfeld, D., Abbassi, A. & YaminiFard, F., 2012. Microseismicity and seismotectonics around the Mosha fault (Central Alborz, Iran), Tectonophysics, **544–545**, 50-59. https://doi.org/10.1016/j.tecto.2012.03.033

Tchalenko, J.S., Berberian, M., Iranmanesh, H., Bailly, M. & Arsovsky, M., 1974. Tectonic framework of the Tehran region. Geological Survey of Iran, Report,

no. 29. https://doi.org/10.1016/0040-1951(75)90169-9

Twardzik, C., Madariaga, R., Das, S. & Custodio, S., 2012. Robust features of the source process for the 2004 Parkfield, California, earthquake from strong-motion seismograms, Geophys. J. Int., **191**, 1245–1254. https://doi.org/10.1111/j.1365-246X.2012.05653.x

Vernant, P., Nilforoushan, F., Hatzfeld, D., Abassi, M.R., Vigny, C., Masson, F., Nankali, H., Martinod, J., Ashtiani, M., Bayer, R., Tavakoli, F. & Chéry, J., 2004. Present-day crustal deformation and plate kinematics in the Middle East constrained by GPS measurements in Iran and northern Oman. Geophysical Journal International **157**, 381–398. https://doi.org/10.1111/j.1365-246X.2004.02222.x

Yagi, Y., Okuwaki, R., Enescu, B. et al., 2016. Rupture process of the 2016 Kumamoto earthquake in relation to the thermal structure around Aso volcano. *Earth Planet Sp,* **68,** 118. https://doi.org/10.1186/s40623-016-0492-3.

Yazdanparast, M. & Vosooghi, B., 2014. A research on Damavand magma source model using GPS data, Geomatics, Natural Hazards and Risk, **5**:1, 26-40, DOI: 10.1080/19475705.2013.772543.

Figures:

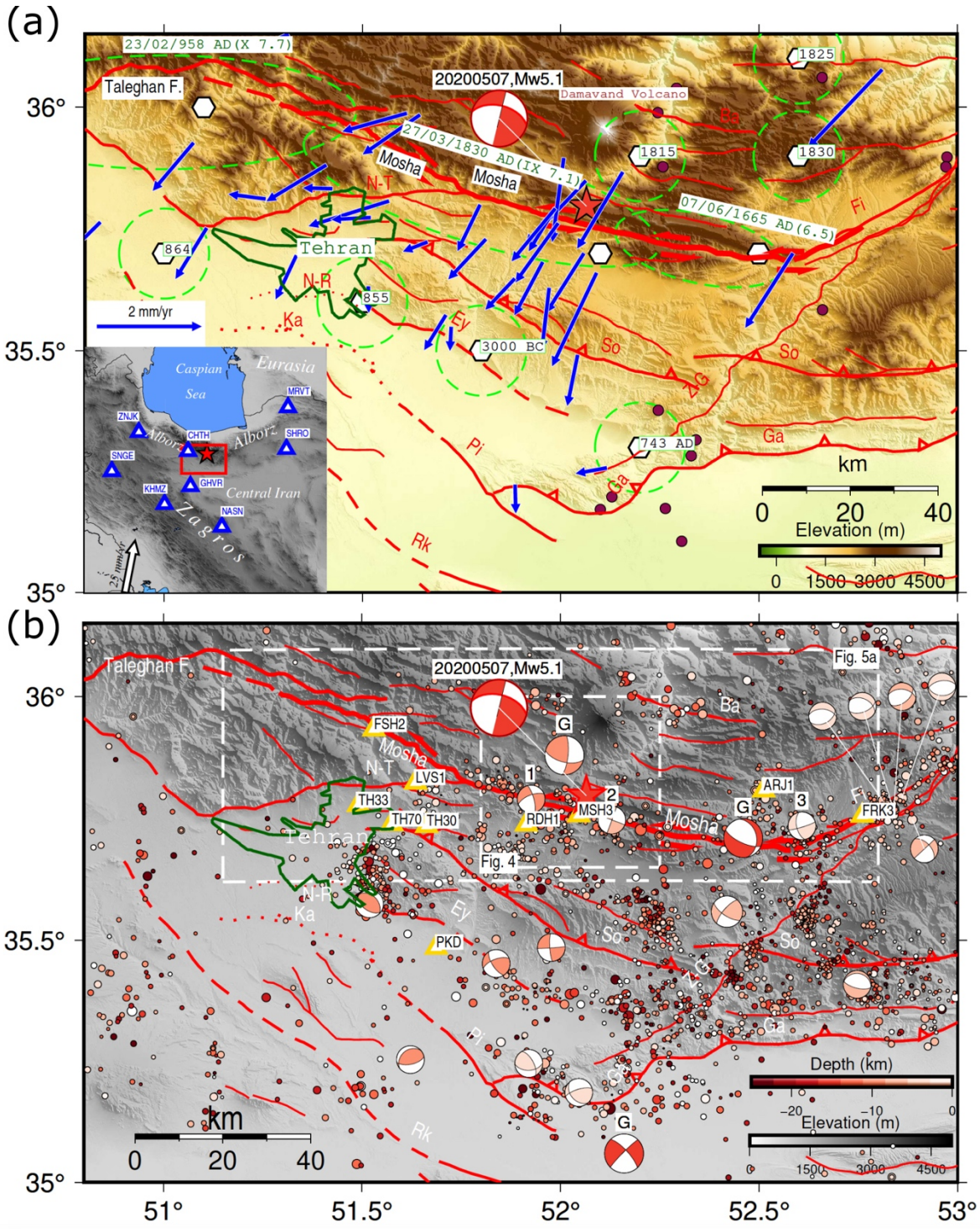
(a)
23/02/958 AD(X 7.7)
Taleghan F.
20200507,Mw5.1
Damavand Volcano
1825
1815
1830
27/03/1830 AD(IX 7.1)
Mosha
N-T
07/06/1665 AD(6.5)
Fi
Ba
864
Tehran
N-R
855
2 mm/yr
Ka
Ey
3000 BC
So
ZG
Pi
743 AD
Ga
Rk
km
0 20 40
Elevation (m)
0 1500 3000 4500
Caspian Sea
Eurasia
Alborz
Central Iran
Zagros
MRVT
ZNJK
CHTH
SHRO
SNGE
GHVR
KHMZ
NASN
36°
35.5°
35°
(b)
Taleghan F.
20200507,Mw5.1
Fig. 5a
FSH2
Mosha
N-T
LVS1
TH33
TH70
TH30
RDH1
MSH3
ARJ1
FRK3
Tehran
Fig. 4
N-R
Ka
Ey
PKD
So
Ba
Ga
Pi
Rk
G
1
2
3
km
0 20 40
Depth (km)
−20 −10 0
Elevation (m)
0 1500 3000 4500
51°
51.5°
52°
52.5°
53°

Figure 1. **a**) Seismotectonics of the study area. Star shows the mainshock hypocenter location and the related focal mechanism as reported by IRSC. Faults are shown with solid and dashed lines. Dotted lines marked N-R and Ka are related to the North-Ray and Kahrizak scarps, respectively, that are uncertain whether created by faulting or are old shorelines (after Nazari et al., 2010). Vectors are geodetic surface deformation rates by Djamour et al., (2010), with respect to a fixed central Iran block. Triangles are the used station data of the Broadband national Iranian Network (BIN) for moment tensor inversion (section 2). Hexagons are historical earthquakes (Ambraseys and Melvile, 1982; Berberian and Yeats, 1999; Nazari et al., 2009). Circles are instrumental earthquakes by Engdahl et al. (2006). Dashed ellipses show affected regions by historical earthquakes. Fault names are: Ga: Garmsar; So: Sorkhe; Ey: Eyvanakey; Fi: Firuzkuh; Pi: Pishva; N-T: North Tehran; Ba: Baijan; Rk: Robat Karim; NR: North Rey. Tehran area is in Green. MSH in red solid line. **b**) Circles: Seismicity recorded by the IRSC network from 2006 until just before the M 5.1 mainshock. Colors represent hypocentral depths. Faults are the same as (a). Focal mechanisms with label G are from the GCMT catalog. The ones without labels and those labeled 1, 2, and 3 are from small to moderate magnitude earthquakes ($3.6<M<4.8$) that occurred from 2006 to 2012 in the region and obtained by inverting local broadband seismic data for their moment tensors (Momeni, 2012). Triangles are the Strong motion stations locations of the Iranian Strong Motion Network (ISMN) that we used their data for extended rupture inversion (section 3).

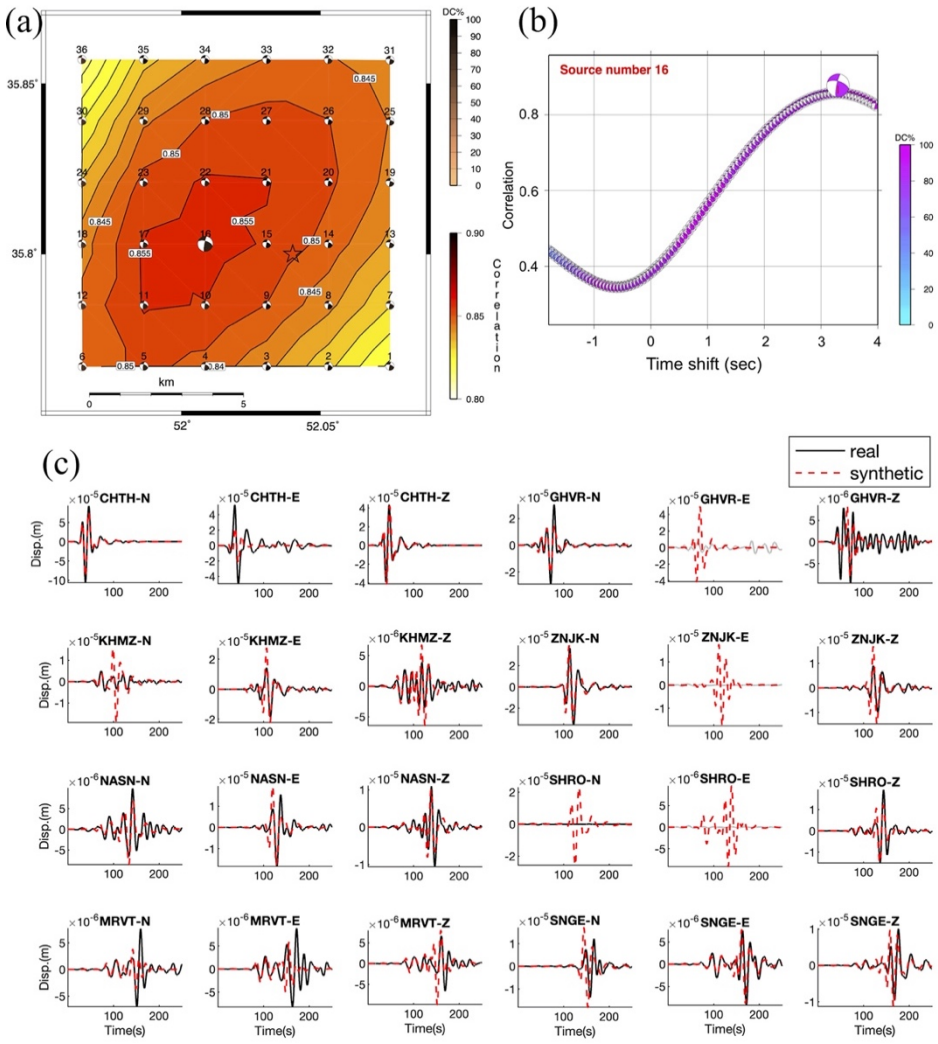

Figure 2. 3D grid search of the M5.1 mainshock centroid location-time. (**a**): Horizontal slice on the space-time correlation plot of trial centroid point sources at a depth of 12 km. The best result was obtained for source number 16 (the larger focal mechanism) with a correlation of 85% situated almost 4 km WNW of the hypocenter reported by IRSC (black star). (**b**): Centroid time correlation plot for the preferred point source #16. The best centroid time has obtained 3.3 s after the IRSC reported origin time. (**c**): Waveform-fit between the real (solid) and synthetic (dashed) displacements for the best obtained moment tensor. Station names-components are written on the top of each sub-figure. Gray waveforms were not used in the inversion, while the related synthetics were produced by forward modeling.

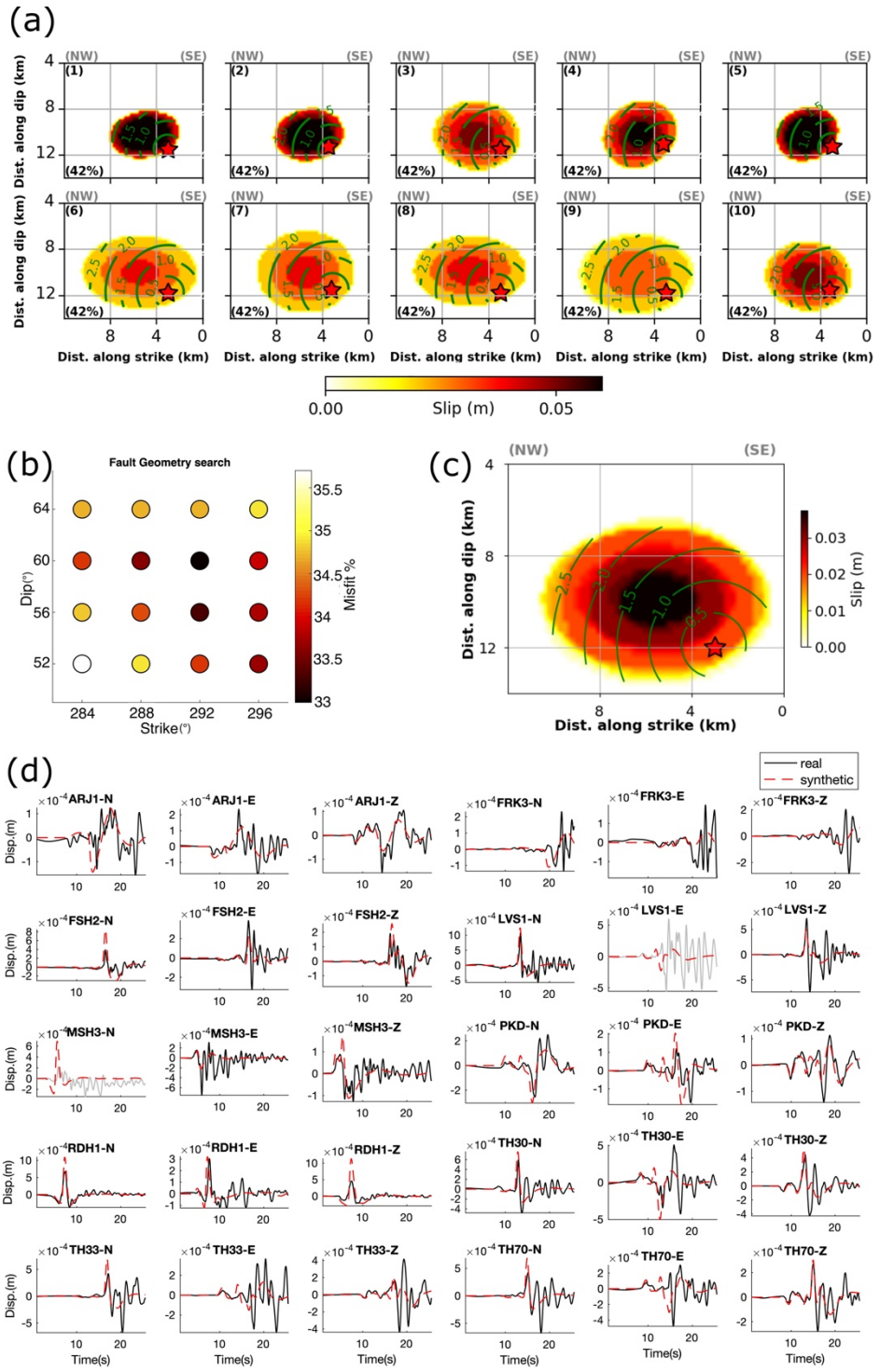
(a)
Dist. along dip (km)
Dist. along strike (km)
(NW)
(SE)
(1)
(2)
(3)
(4)
(5)
(6)
(7)
(8)
(9)
(10)
(42%)
0.00
Slip (m)
0.05
(b)
Fault Geometry search
Dip(°)
Strike(°)
Misfit %
(c)
Dist. along dip (km)
Dist. along strike (km)
Slip (m)
(d)
real
synthetic
ARJ1-N
ARJ1-E
ARJ1-Z
FRK3-N
FRK3-E
FRK3-Z
FSH2-N
FSH2-E
FSH2-Z
LVS1-N
LVS1-E
LVS1-Z
MSH3-N
MSH3-E
MSH3-Z
PKD-N
PKD-E
PKD-Z
RDH1-N
RDH1-E
RDH1-Z
TH30-N
TH30-E
TH30-Z
TH33-N
TH33-E
TH33-Z
TH70-N
TH70-E
TH70-Z
Disp.(m)
Time(s)

Figure 3. **(a)**: 10 final rupture models for the mainshock obtained on the preferred geometry obtained during independent inversions, assuming different ranges for the rupture parameters. (**b**): Grid-search of the geometry of the ruptured area. The preferred geometry has a strike/dip of 292°/60°. (**c**): The best rupture model for the mainshock. (**d**): waveform-fit of the best rupture model shown in c. Gray waveforms were not used in the inversion, their corresponding synthetic waveforms were obtained by forward-modeling.

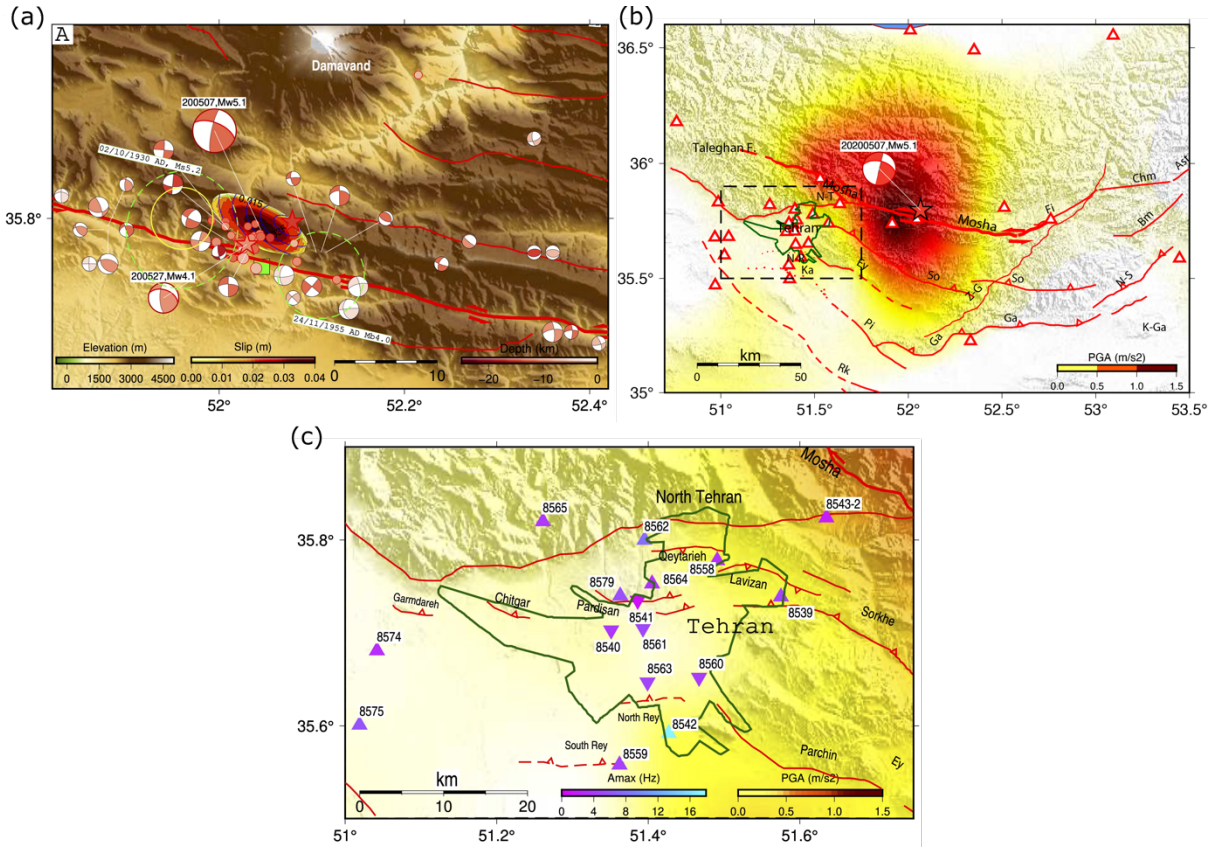

Figure 4. **a**) Correlation between mainshock rupture (colored ellipses is the surface projection of rupture) and aftershocks of the first 45 days (filled circles). Stars are mainshock and largest aftershock hypocenters relocated in this study (section 3). The mainshock focal mechanism is obtained in section 2. The M4.1 27/05/2020 aftershock focal mechanism is from IRSC. Inner colors represent their depths. Faults are plotted with red lines. curved lines on the rupture model represent rupture direction. The square is the location of Mosha town. The dashed ellipses show the damaged areas of the Ms 5.2 1930 and Mb 4.0 1955 earthquakes (after Berberian et al., 1993). Other focal mechanisms are from microearthquakes on the MSH obtained by Tatar et al. (2012) from June to October 2006. The solid circle is the observed thermal area on the MSH

(after Eskandari et al., (2018). **b**) The directivity effect of the 7th May Mw5.1 mainshock observed from the PGA recorded in the triggered BHRC network stations in the region. Strong motion stations are shown in triangles. The black dashed rectangle shows the area shown in (c). **(c)** PGA distribution of the mainshock in the Tehran area**.** Solid lines are the active faults (after Talebian et al., (2016)). Strong motion stations inside Tehran city are shown in reverse triangles. Inner colors of triangles represent the maximum spectral frequency (Amax) at the stations. Dashed lines are probable shore-line scarps (after Nazari et al., 2010).

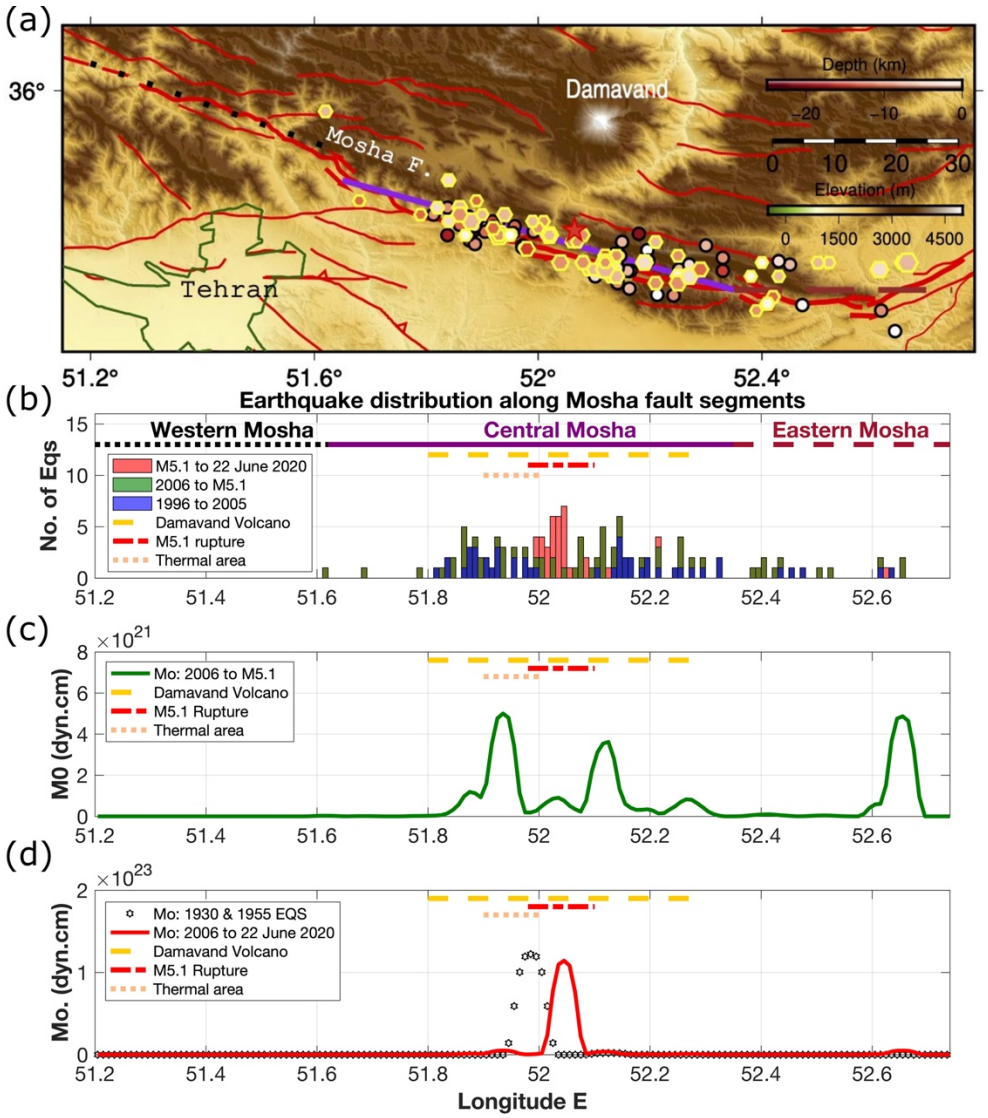

Figure 5. (**a**): Seismicity in a distance of 5 km of the MSH from 1996 until the M5.1 mainshock. Circles and hexagons are the earthquakes from 1996 to the end of 2005, and 2006 until before the M5.1, respectively. Dotted, solid, and dashed lines are Western, Central, and Eastern segments of the MSH, respectively. **(b)**: Histogram showing the distribution of earthquakes along the MSH. **(c)**: Distribution of scalar seismic moments along the MSH from 2006 until before the 2020 M5.1 mainshock. **(d)**: Distribution of scalar seismic moments along MSH from 2006 until 22 June 2020, including the M5.1 mainshock and 27 M>=2.5 early aftershocks.

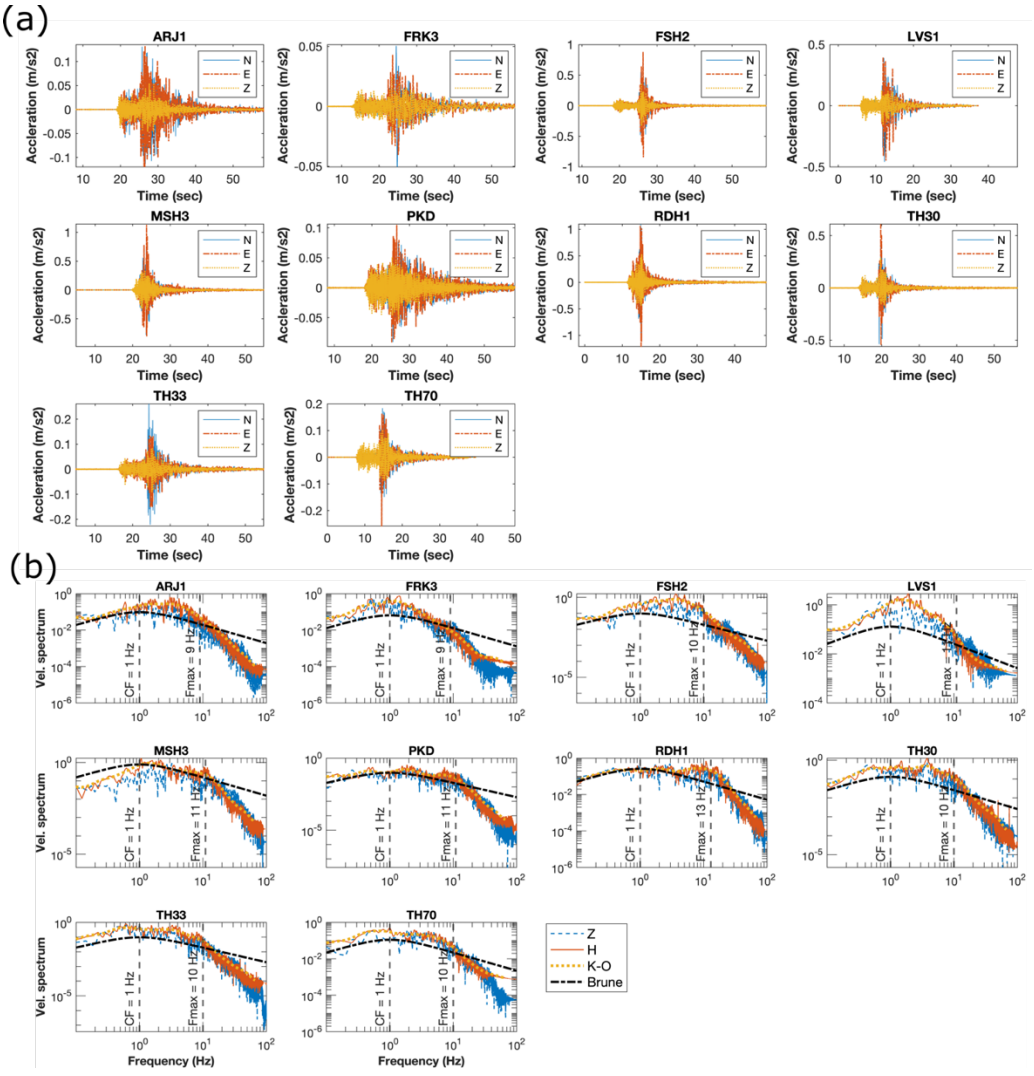

Figure 6. (**a**) Strong motion signals of the mainshock recorded in the near-field stations shown in Figure 1b. (**b**) The Fourier spectra of the strong motions

showed in (a). Black dashed line represents the Brune theoretical velocity spectra for a circular source.

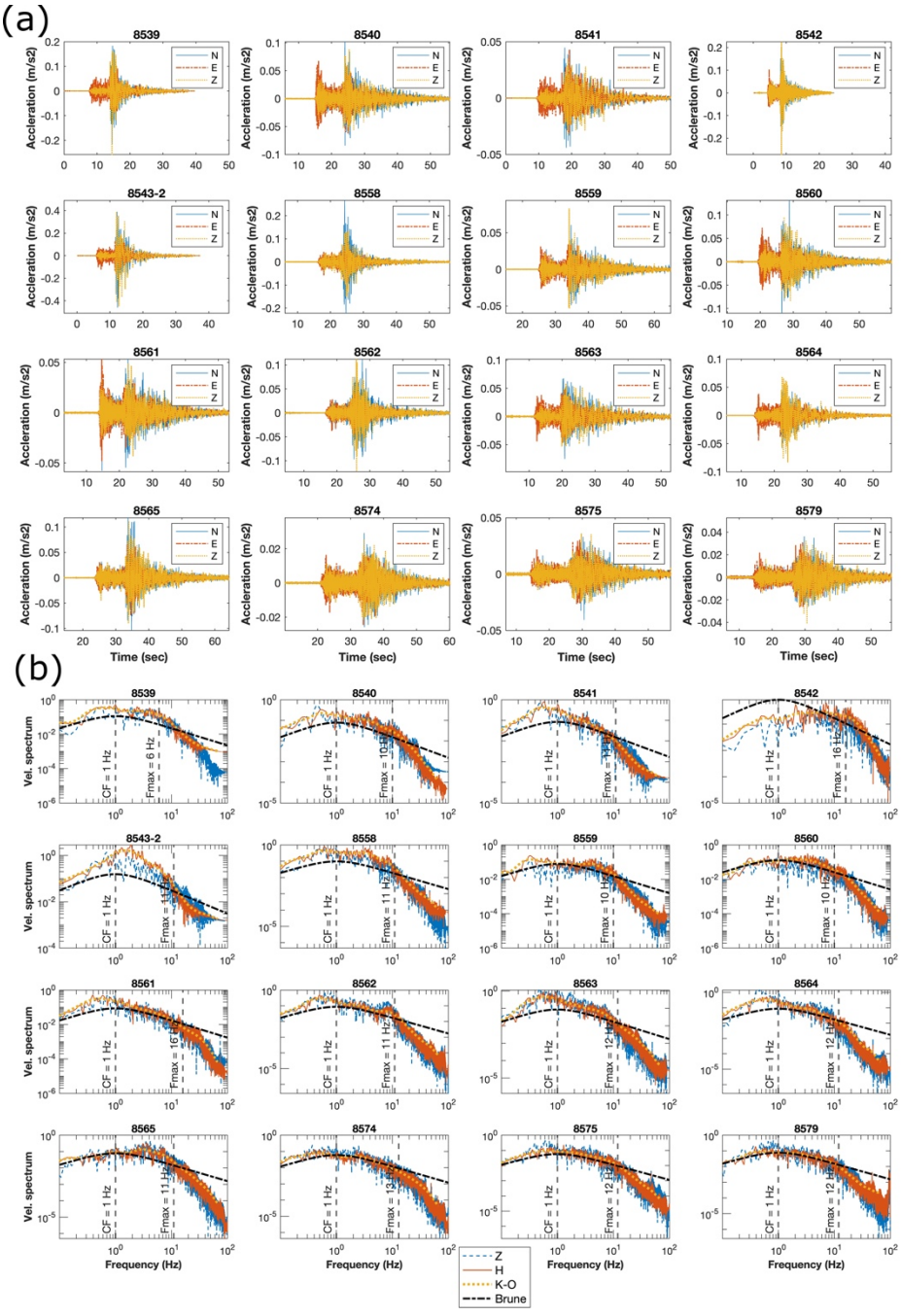

Figure 7. (**a**) Strong motion acceleration waveforms of the mainshock recorded in the ISMN network stations in the Tehran area shown in Figure 4c. (**b**) The velocity Fourier spectra of the strong motions shown in (a). Black dashed line represents the Brune theoretical velocity spectra for a circular source.

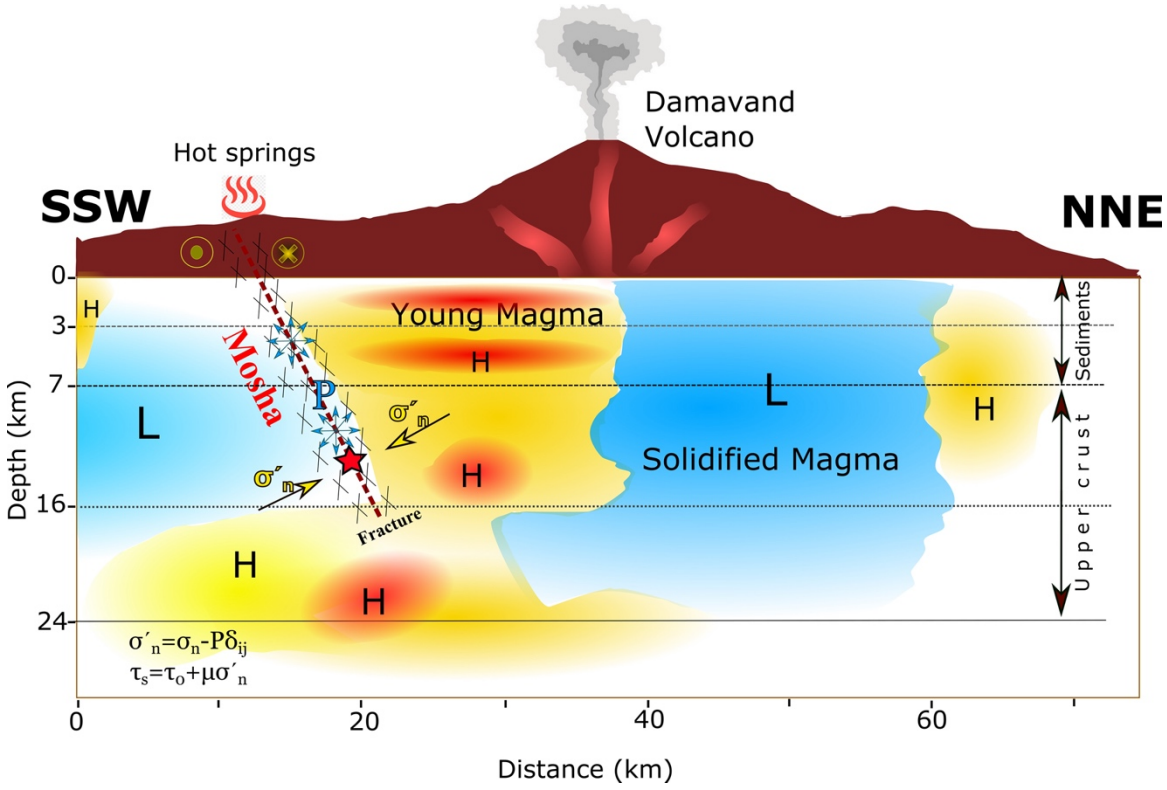

Figure 8. Schematic plot illustrating the relation between MSH and DMV. Red and Blue represent the hot and cool rocks, respectively (after Mostafanejad et al., 2011, Shomali and Shirzad, 2014, Yazdanparast and Vosooghi, 2014, Vajedian et al., 2015, Eskandari et al., 2018). Star is the 7 May 2020 M5.1 mainshock hypocenter. H and L represent high and low temperature areas, respectively. The dashed line is the MSH. Horizontal thin dashed lines are crustal velocity layers from Tatar et al., (2012).